ACS Biomaterials SCIENCE & ENGINEERING
Article
Cite This: ACS Biomater. Sci. Eng. 2018, 4, 1397−1406

Biodegradable Water-Based Polyurethane Shape Memory Elastomers for Bone Tissue Engineering

Yu-Jen Wang,[†] U-Ser Jeng,[‡] and Shan-hui Hsu*[,†,§,∥]

[†]Institute of Polymer Science and Engineering, National Taiwan University, No. 1 Sec. 4 Roosevelt Road, Taipei 10617, Taiwan, R.O.C.

[‡]National Synchrotron Radiation Research Center, Hsinchu Science Park, No. 101 Hsin-Ann Road, Hsinchu 30076, Taiwan, R.O.C.

[§]Research and Development Center for Medical Devices, National Taiwan University, No. 1 Sec. 4 Roosevelt Road, Taipei 10617, Taiwan, R.O.C.

[∥]Institute of Cellular and System Medicine, National Health Research Institutes, No. 35 Keyan Road, Miaoli 35053, Taiwan, R.O.C.

Supporting Information

ABSTRACT: Shape memory polymers (SMPs) are polymers with the shape memory effect. The biodegradable SMPs are candidate materials for making biomedical devices and scaffolds for tissue engineering. Superparamagnetic iron oxide nanoparticles (SPIO NPs) have recently been reported to promote the osteogenic induction of human mesenchymal stem cells (hMSCs). In this study, we synthesized water-based biodegradable shape memory polyurethane (PU) as the main component of the 3D printing ink for fabricating bone scaffolds. The 3D printing ink contained 500 ppm of SPIO NPs to promote osteogenic induction and shape fixity, and it also contained polyethylene oxide (PEO) or gelatin for the improvement of printability. Scaffolds were printed by the microextrusion-based low-temperature fuse deposition manufacturing (LFDM) platform. Both PU−PEO and PU−gelatin ink showed excellent printability. Shape memory properties were evaluated in 50 °C air and 37 °C water. PU−PEO scaffolds showed better shape fixity and recovery than PU−gelatin scaffolds, while the shape memory properties in water were better than those in air. hMSCs were seeded for evaluation of bone regeneration. The proliferation of the hMSCs in PU/gelatin and PU/gelatin/SPIO scaffolds was greater than that in PU/PEO and PU/PEO/SPIO scaffolds, confirming the better compatibility of gelatin vs PEO as the viscosity enhancer of the ink. The gradual release of SPIO NPs from the scaffolds promoted the osteogenesis of seeded hMSCs. With SPIO in the scaffolds, the osteogenesis increased 2.7 times for PU/PEO and 1.5 times for PU/gelatin scaffolds based on the collagen content. Meanwhile, SPIO release from PU/PEO/SPIO scaffolds was faster than that from PU/gelatin/SPIO scaffolds at 14 days, consistent with the better osteogenesis observed in PU/PEO/SPIO scaffolds. We concluded that 3D printed PU scaffolds with shape memory properties, biodegradability, and osteogenic effect may be employed to the minimally invasive surgical procedures as customized-bone substitutes for bone tissue engineering.

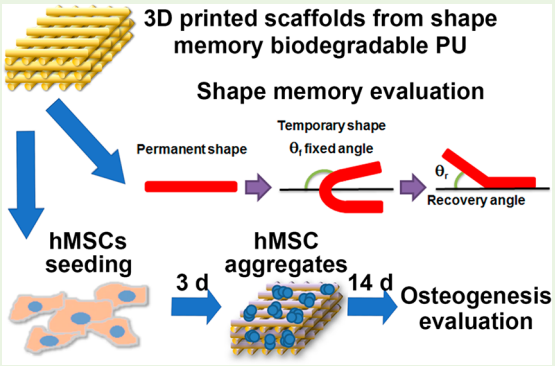

KEYWORDS: *shape memory polyurethane elastomer, superparamagnetic iron oxide, 3D printed scaffold, bone tissue engineering, mesenchymal stem cells (MSCs)*

1. INTRODUCTION

Shape memory materials are materials that can be fixed at a temporary shape by physical or chemical methods. Upon stimulation, they can recover to the permanent shape.[1] Shape memory polymers (SMPs) are polymers with the shape memory effect. Because of the tunable mechanical properties and biodegradability, SMPs are candidates for biomedical devices and scaffolds for tissue engineering.[2] SMPs have been developed for clot removal devices,[3] vascular stents,[4] sutures,[5] and orthodontic appliances.[6] In the field of tissue engineering, the biodegradable SMP scaffolds can be seeded with cells and implanted into the tissue injury site by minimally invasive surgical procedures. The development of minimally invasive surgical procedures in surgical medicine has ameliorated the health care during the past few decades.[5] Advantages of minimally invasive surgery include the reduction of surgical trauma and reduction of pain medication usage.[7] When SMP scaffolds are implanted through the minimally invasive surgery, the wound recovers faster and the scaffolds degrade with time without a second surgery.[8]

Three-dimensional (3D) printing is a rapid fabrication method with layer-by-layer additive manufacturing. Customized

Received: January 26, 2018
Accepted: February 21, 2018
Published: March 7, 2018

Downloaded via NATL TSING HUA UNIV on January 21, 2019 at 05:31:12 (UTC).
See https://pubs.acs.org/sharingguidelines for options on how to legitimately share published articles.

© 2018 American Chemical Society

DOI: 10.1021/acsbiomaterials.8b00091
ACS Biomater. Sci. Eng. 2018, 4, 1397−1406

scaffolds can be made through the computer-aided design (CAD) system.[9] Lately, scaffolds for bone tissue engineering have been fabricated by 3D printing. Inzana et al.[10] produced calcium phosphate scaffolds by 3D printing as bone graft substitutes, which were optimized for biocompatibility, osteoconductivity, and mechanical properties, and were further implanted into murine femoral defects for 9 weeks. Tarafder et al.[11] applied 3D printing to manufacture 3D interconnected macroporous tricalcium phosphate scaffolds, which were found to facilitate osteoid-like new bone formation in rat femoral defects. However, these ceramic scaffolds are generally brittle and degrade slowly. To choose the printing materials with biodegradability as well as shape memory effect, polyurethane meets the requirements. The degradation rate and mechanical properties of polyurethane can be adjusted by the soft segment species and ratios.[12] Waterborne polyurethane can be prepared by environmental-friendly processes without the use of organic solvent. The aqueous dispersion of biodegradable polyurethane was employed to fabricate cartilage tissue engineering scaffolds by 3D printing.[13] Biodegradable waterborne polyurethane with shape memory effect has been recently synthesized.[14] These findings suggested that waterborne polyurethane may be a good candidate material to make 3D-printed SMP for tissue engineering applications.

Bone tissue engineering involves a complex dynamic process, including the migration, proliferation, differentiation of osteoprogenitors, and the formation of extracellular matrix (ECM).[15] Synthetic and biodegradable SMP scaffolds have been explored for bone tissue engineering. Bao et al.[16] fabricated poly(D,L-lactide-*co*-trimethylene carbonate) shape memory porous scaffolds with biodegradability. The osteoblasts cultured on scaffolds could proliferate and show bone mineral precipitation. Nanoparticles (NPs) have been used to stimulate bone regeneration. Superparamagnetic iron oxide nanoparticles (SPIO NPs) widely used for hyperthermia treatment, cell tracking, and magnetic resonance imaging[17−19] have recently been reported to promote the osteogenic induction of human-bone-derived mesenchymal stem cells (hBMSCs).[20] When SPIO NPs were added in polyurethane, the nanocomposites showed better shape memory effect than the original polymer.[21,22]

In this study, we synthesized biodegradable water-based shape memory polyurethane (abbreviated as PU) as the main component of the 3D printing ink for fabricating bone scaffolds. The 3D printing ink also contained SPIO NPs to promote osteogenic induction and shape fixity and contained polyethylene oxide or gelatin for the improvement of printability. Scaffolds were printed by the low-temperature fuse deposition manufacturing (LFDM) platform. Shape memory effect of the scaffolds was first evaluated. The 3D printed scaffolds seeded with hBMSCs were then analyzed for their potential for bone tissue engineering. By combining the shape memory performance and 3D printing, we expected to develop novel customized scaffolds for use in the minimally invasive surgical procedures and applications in bone tissue engineering.

2. MATERIALS AND METHODS

2.1. Synthesis of Polyurethane and Superparamagnetic Iron Oxide Nanoparticles (SPIO NPs). The polyurethane used in this study was synthesized from an optimized waterborne procedure[23] as shown in Figure 1A. The composition of this polyurethane was determined from a previous work.[23] The soft segment contained

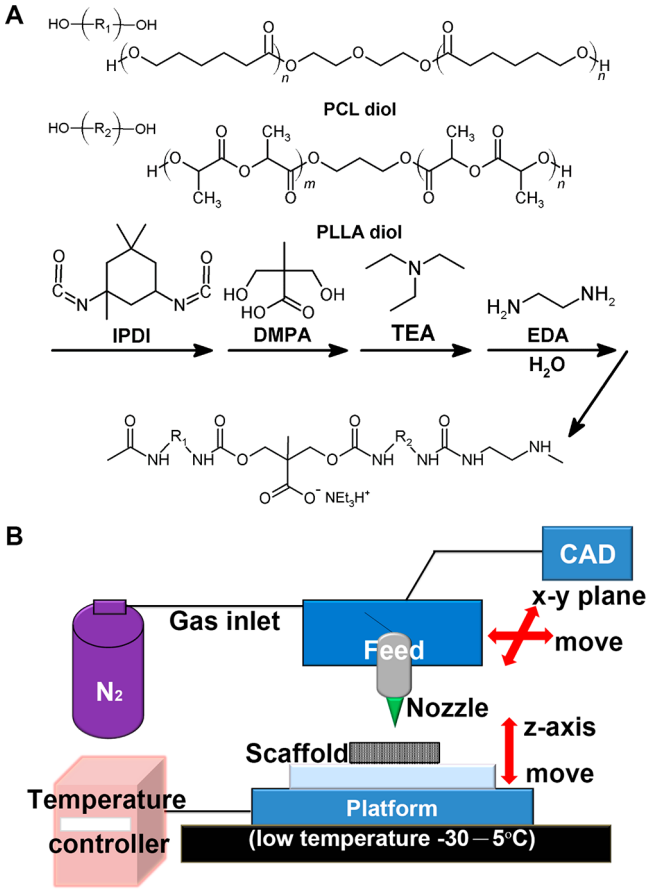

Figure 1. Schematics showing (A) the preparation of shape memory biodegradable polyurethane elastomer and (B) the fabrication of shape memory scaffolds by 3D printing using a low-temperature fuse deposition manufacturing (LFDM) platform. The platform was set at −30 °C for PU/PEO ink and 5 °C for PU/gelatin ink in the study.

poly(ε-caprolactone) diol (PCL diol, Mn = 2000 Da; Sigma) and poly(L-lactic acid) diol (PLLA diol, Mn = 2000 Da) in a molar ratio of 6:4. The isocyanate was isophorone diisocyanate (IPDI, Acros). The chain extenders were 2,2-bis(hydroxymethyl)propionic acid (DMPA, Sigma) and ethylenediamine (EDA, Tedia). Triethylamine (TEA, J. T. Baker) was added to neutralize DMPA in aqueous dispersion. The dispersion was prepared from the waterborne synthesis of polyurethane, including the use of self-emulsifying chain extender (DMPA) and vigorous stirring. This polyurethane was abbreviated as "PU" in the experiment and data presentation. SPIO NPs were synthesized by the co-precipitation method described in a previous study[24] as shown in Figure S1A in Supporting Information. The morphology and size distribution of SPIO NPs were observed by a transmission electron microscope (TEM, JEOL, Japan). Samples for TEM were made by SPIO NPs water dispersion dropped on the surface of copper grids. The hydrodynamic diameter was measured by the DelsaNano ζ potential and submicrometer particle size analyzer (Beckman Coulter, USA). The weight profile of SPIO NPs was obtained by a themogravimetric analyzer (TGA, Q50, TA Universal, USA) under nitrogen atmosphere at a heating rate of 20 °C/min.

2.2. Preparation of Films and Freeze-Dried Scaffolds. PU solid films were prepared by casting PU dispersion on Teflon mold and removal of the residual solvent by vacuum. To prepare PU and PU/SPIO freeze-dried scaffolds, PU and PU/SPIO dispersions were frozen in a −20 °C refrigerator for 24 h and freeze-dried in vacuum for another 24 h (abbreviated as FD scaffolds).

2.3. Fabrication of Scaffolds by 3D Printing. The waterborne PU dispersion was the main component of 3D printing ink. To enhance the viscosity, polyethylene oxide (PEO, Mn = 900 kDa;

DOI: 10.1021/acsbiomaterials.8b00091
ACS Biomater. Sci. Eng. 2018, 4, 1397−1406

Scientific Polymer) was dissolved in water (10% w/w) and mixed with PU in the final weight ratio of 24:76 (PEO/PU) as the ink used for 3D printing. Alternatively, gelatin type A (from porcine, 300 bloom; Sigma) was dissolved in water (7.7% w/w) and mixed with PU in the final weight ratio of 15:85 (gelatin/PU). To prepare the scaffolds containing SPIO NPs, the ink described above was further mixed with SPIO NPs, so the final scaffolds contained 500 ppm of SPIO NPs. The solid content of all ink formulas was 20 wt %. Scaffolds were fabricated by a Regenovo 3D bioprinter (Regenovo Biotechnology) with a low-temperature fuse deposition manufacturing (abbreviated as LFDM) platform. The 3D bioprinter comprising the computer-aided design (CAD) system, $x-y-z$ motion platform, cooling system, nozzle, and temperature and pressure controllers is shown in Figure 1B. The nozzle size used in this study was 210 μm. The extrusion pressure was 40−250 kPa depending on the ink. The scaffolds were printed layer-by-layer with fibers deposited on the low temperature platforms based on CAD structure, followed by freeze-drying for 24 h. The 3D printed scaffolds were abbreviated as 3DP scaffolds in the study.

2.4. Physicochemical Characterization of Scaffolds. Differential scanning calorimetry (DSC), X-ray diffraction (XRD), scanning electron microscopy (SEM), and dynamic mechanical analysis (DMA) were performed to characterize the scaffolds as described below.

The crystallinity, melting points, and heat flow of FD and 3DP scaffolds were measured by DSC (Q20, TA Universal, USA). Samples weighing about 3 mg in an aluminum pan were cooled from 40 °C to −70 °C at a cooling rate of 10 °C/min and heated to 140 °C at a heating rate of 10 °C/min with nitrogen purging for DSC measurement. The diffraction peaks of each FD and 3DP scaffolds were determined by XRD (X'Pert, PANalytical, The Netherlands) with Cu Kα radiation (40 kV, 40 mA). The intensity was detected from 10° to 30° at a speed of 0.02°/s under room temperature. The morphology and porous structure of 3DP scaffolds were observed by SEM (TM-3000, Hitachi). The average pore diameter was obtained by image analysis. The mechanical properties of 3DP scaffolds were measured by DMA (Q800, TA Universal, USA) in the compression mode at 0.1% strain and 1 Hz of frequency under 37 °C.

The degradation of FD and 3DP scaffolds was also evaluated. Scaffolds were placed in the phosphate buffer saline (PBS) under 37 °C. After 7, 14, 21, and 28 days, the scaffolds were washed by deionized distilled water and dried in vacuum for 24 h to weigh (designated as W_f). The percent remaining weight was calculated by the following equation: remaining weight (%) = $W_f/W_i \times 100$, where W_i was the weight at 0 day before soaking. In addition, the accumulative release of SPIO NPs from SPIO containing scaffolds immersed in PBS was determined by an atomic absorption spectrometer (AA, iCE-3000, ThermoFisher Scientific, USA).

2.5. Evaluation of Shape Memory Performance of the FD and 3DP Scaffolds. Shape memory effect of scaffolds was evaluated by the U-bending test.[25] The samples were cut into 20 mm in length, 5 mm in width, and 0.2 mm in thickness. First, the samples were put into a 50 °C oven for 30 min and deformed to the U shape. Second, the samples were put into a −10 °C refrigerator for 5 min, and the fixed angle θ_f was measured after maintaining at 25 °C for 1 min. Third, the samples were put into a 50 °C oven for 5 min, and the recovery angle θ_r was measured after maintaining at 25 °C for 1 min. The evaluating procedures in water were similar to those in air except that the 50 °C oven treatment was replaced by 37 °C water treatment. The fixity ratio and recovery ratio were defined as the equations below.

$$\text{shape fixity ratio } (\%) = \frac{\theta_f}{180} \times 100 \quad (1)$$

$$\text{shape recovery ratio } (\%) = \frac{\theta_f - \theta_r}{\theta_f} \times 100 \quad (2)$$

2.6. Viability of Human Mesenchymal Stem Cells (hMSCs) in 3DP Scaffolds. hMSCs were isolated from human bone marrow[26] and cultured in low-glucose Dulbecco's modified Eagle's medium (DMEM, Gibco) with 10% fetal bovine serum (FBS, Gibco), 1% penicillin streptomycin (Gibco), and 3.7 g/L sodium bicarbonate ($NaHCO_3$, Sigma) in 37 °C, 5% CO_2 incubator. The medium was refreshed once every 3 days.

The scaffolds were sterilized in UV light for 24 h. 100 μL of cell suspension (density 10^7 cells/mL) was dripped on the top center of each scaffold. The seeded scaffolds were incubated in a 6-well tissue culture plate for 4 h, and then 3 mL of fresh culture medium was added. To observe the cell morphology in the scaffolds, a red fluorescent dye PKH26 (Sigma, USA) was used to label cells. First, hMSCs were washed with PBS and resuspended in the labeling solution containing 1 μL of liquid PKH26 and 200 μL of dilution buffer and reacted for 2 min. The reaction was ended by the culture medium. Cell morphology was observed under an inverted fluorescence microscope (Leica, DMIRB, Germany).

The cell viability in the scaffolds was calculated according to the DNA content using the Hoechst 33258 fluorescent dye assay.[27] The samples were treated with freezing−thawing cycles between −80 °C and 37 °C three times, and reacted with Hoechst 33258 dye for 1 h avoiding light. The fluorescence intensity was measured by fluorescence spectroscopy with an excitation of 365 nm and an emission of 458 nm (SpectraMax M5 microplate reader, Molecular Devices). The cell number was determined based on a standard curve constructed from known numbers of hMSCs. The initial cell number (0 h) was determined after the cells were seeded to scaffolds for 4 h before the addition of fresh medium. After that, cell number was counted at 24 h, 48 h, 72 h, and 14 days.

2.7. Osteogenic Induction for hMSCs Seeded in 3DP Scaffolds. Osteogenic induction was performed by culturing the hMSCs-seeded scaffolds in osteogeneic medium which was low glucose-DMEM containing 10% FBS, 0.2 mM of L-ascorbate-2-phosphate (Sigma), 10 mM β-glycerophosphate (Sigma), and 10^{-5} mM dexamethasone (Sigma). After being cultured for 3 days in basal medium, the hMSCs-seeded scaffolds were then cultured in the osteogenic induction medium for 7 and 14 days.

The gene expression of osteogenic markers including alkaline phosphatase (ALP), runt related transcription factor 2 (RUNX2), osteocalcin (OCN), and collagen type I (COL I) was analyzed by the quantitative reverse transcriptase-polymeric chain reaction (qRT-PCR) using a Chromo 4 PTC200 thermal cycler (MJ Research, USA) and the DyNAmo Flash SYBR Green qPCR kit (Finnzymes Oy, Espoo, Finland). The gene expression levels were calculated and normalized to glyceraldehyde 3-phosphate dehydrogenase (GAPDH) in the same sample.

The mineral deposition in 3DP scaffolds was determined by Alizarin red staining assay.[28] The cells on the scaffolds were fixed with 4% paraformaldehyde for several minutes and then immersed in 1% Alizarin red S (Sigma-Aldrich) solution (pH = 4.3) for 30 min at 22 °C. The scaffolds were washed with PBS and examined with optical microscopy. Meanwhile, some of the 3DP scaffolds were immersed in 3% nitric acid (Showa, Japan) for 24 h to dissolve calcium deposition for calcium content analysis by AA. The collagen content of the hMSCs-seeded 3DP scaffolds was determined by the proline assay,[29] using the UV/vis spectroscopy (SpectraMax M5 microplate reader, Molecular Devices) after reaction with p-dimethylaminobenzaldehyde. The concentration of the L-hydroxyproline was calculated based on a standard curve constructed from known concentrations of the L-hydroxyproline and was converted to the collagen content.[30]

2.8. Statistical Analysis. The experiment performed in this study was reproduced independently three times. Data were expressed as the mean ± standard deviation (n = 3). The statistical variance of each group was analyzed by one-way ANOVA. Data with p values of <0.05 were considered statistically significant.

3. RESULTS

3.1. Synthesis of PU and SPIO NPs and Fabrication of Scaffolds. The waterborne biodegradable PU elastomer was synthesized as the water dispersion, serving as the base of 3D printing ink as shown in Figure 1A. SPIO NPs were synthesized by co-precipitation and dispersed in water by surface modification with sodium oleate as shown in Figure S1A.

DOI: 10.1021/acsbiomaterials.8b00091
ACS Biomater. Sci. Eng. 2018, 4, 1397−1406

The morphology of the SPIO NPs used in this study is shown in Figure S1B. The shape of the SPIO NPs was round with an average diameter of 5.7 ± 1.98 nm. The chemical composition (inorganic/organic fraction) of SPIO NPs was defined by TGA displayed in Figure S1C. The ratio of SPIO and the surfactant was 45:55. The hydrodynamic diameter of SPIO analyzed by DLS was 85.6 ± 0.48 nm.

The PU dispersion was blended with PEO or gelatin to adjust the viscosity suitable for printing. The 3D printing was operated through a LFDM platform as illustrated in Figure 1B. The geometry of the scaffolds was designed as rectangular through CAD with dimensions of 10 × 10 × 2.5 mm^3 for all the 3DP scaffolds. The optimized parameters for printing PU/PEO and PU/PEO/SPIO were at the extruding pressure 220 kPa on the −30 °C platform with a velocity of 9.0 mm/s. The optimized parameters for printing PU/gelatin and PU/gelatin/SPIO were at the extruding pressure 120 kPa on the 5 °C platform with a velocity of 7.0 mm/s. The 3D printed scaffolds were followed by freeze-drying for 24 h. The final scaffolds are shown in Figure 2. The dimension of the square in PU/PEO and PU/PEO/SPIO scaffolds shrank from 10 mm to 9 mm and 8.5 mm, and that in PU/gelatin and PU/gelatin/SPIO both shrank from 10 mm to 9 mm. The thickness of scaffolds shrank from 2.5 mm to 2.45 mm in PU/PEO and PU/PEO/SPIO scaffolds, and that in PU/gelatin and PU/gelatin/SPIO shrank from 2.5 mm to 2.42 mm. After immersion in 37 °C water, the dimension of the square in PU/PEO/SPIO and PU/gelatin/SPIO scaffolds (~15% shrinkage) recovered approximately to the original design, while PU/PEO and PU/gelatin (~10% shrinkage) showed less dimensional recovery. The thickness did not show significant recovery. The surface of the stacking fibers in 3DP scaffolds is shown in Figure S2. The microporous structure was observed in each stacking fiber of PU/PEO, PU/PEO/SPIO, or PU/gelatin/SPIO scaffolds. The pore size on the surface of the fiber was 6.6 ± 1.14 μm for PU/PEO scaffolds, 1.5 ± 0.54 μm for PU/PEO/SPIO scaffolds, and 5.2 ± 1.68 μm for PU/gelatin/SPIO scaffolds based on an average of >50 pores. Meanwhile, there was no obvious surface porosity in the stacking fibers of PU/gelatin scaffolds.

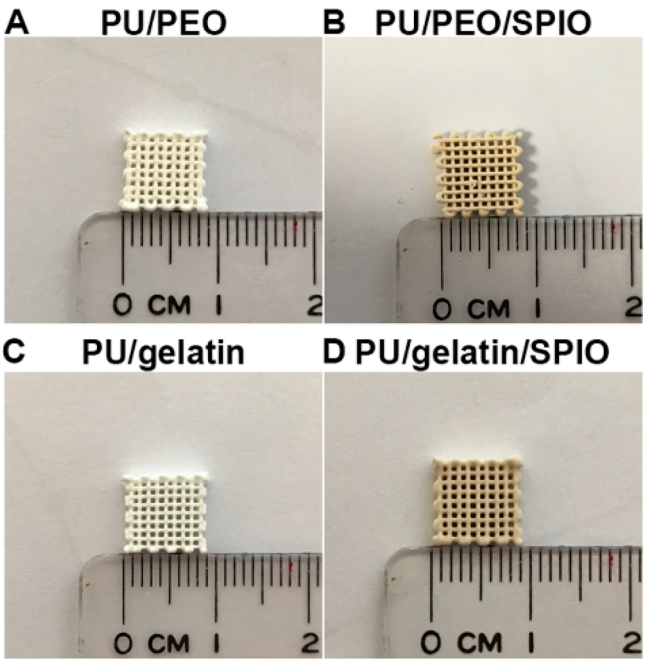

Figure 2. (A–D) Structures of 3DP scaffolds. The ratio of PEO or gelatin was optimized for printing. The microporous structure of the stacking fibers is shown in Figure S2.

3.2. Crystallinity Analysis of FD Scaffolds and 3DP Scaffolds. The DSC curves of the scaffolds are shown in Figure 3. The endothermic peaks in 48–55 °C and in 116–137 °C represented the crystallinity of PCL and PLLA, respectively. The endothermic peaks at around 65 °C in PU/PEO and PU/PEO/SPIO 3DP scaffolds represented the crystallinity of PEO. The melting temperature (T_m) of PCL and PLLA is listed in Table 1. The T_m of the scaffolds was influenced by the composition. The addition of PEO and SPIO NPs increased the T_m of PCL, while the addition of gelatin and PEO decreased that of PLLA. The melting peaks of PCL could not be clearly observed in PU/PEO/SPIO 3DP scaffolds because of the overlapping of the melting peaks for PCL and PEO. The XRD profiles are shown in Figure 4. The diffraction peaks were assigned to PLLA at 16.5° and 18.9°, to PCL at 21.0° and 23.0°, and to PEO at 23.7° and 26.5°. The crystallinity of each scaffold was calculated and is summarized in Table 1. PU/gelatin 3DP scaffolds had lower crystallinity than PU FD scaffolds, while PU/PEO 3DP scaffolds had higher crystallinity. The addition of SPIO NPs elevated the extent of crystallinity for each FD or 3DP scaffold.

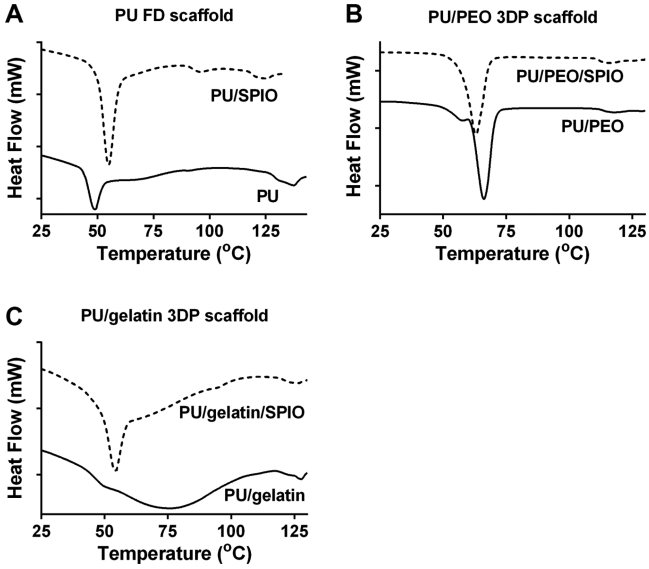

Figure 3. DSC profiles for (A) PU and PU/SPIO FD scaffolds, (B) PU/PEO and PU/PEO/SPIO 3DP scaffolds, and (C) PU/gelatin and PU/gelatin/SPIO 3DP scaffolds. SPIO accounted for 500 ppm of the total weight in each scaffold.

3.3. Dynamical Mechanical Properties of the 3DP Scaffolds. The dynamical mechanical properties at 37 °C evaluated by DMA in the compression mode are shown in Table 2. The storage modulus (E') of PU/PEO scaffolds was higher than that of PU/gelatin because the total degree of crystallinity for PU/PEO was higher than that of PU/gelatin. The presence of SPIO NPs increased both E' and E'' for PU/PEO and PU/gelatin 3DP scaffolds. The tan δ of PU/PEO was higher than that of PU/gelatin and was increased by the addition of SPIO NPs in both scaffolds. To simulate the modulus of the 3DP scaffolds at the wet state, the scaffolds were immersed in 37 °C PBS for 1 h and evaluated again. The

DOI: 10.1021/acsbiomaterials.8b00091
ACS Biomater. Sci. Eng. 2018, 4, 1397–1406

Table 1. Thermal Properties and Crystallinity Measured by DSC and XRD

	DSC				XRD
sample	PCL T_m (°C)	PLA T_m (°C)	heat flow (J/g)	crystallinity (%)	crystallinity (%)
PU FD	48.5	137.4	10.4	8.89	9.35
PU/SPIO FD	54.9	125.2	23.1	17.5	18.1
PU/PEO 3DP	55.5	116.7	33.0	23.4	16.9
PU/PEO/SPIO 3DP	62.1 (PEO)	122.1	52.6	37.0	22.3
PU/gelatin 3DP	48.8	127.6	3.31	3.75	6.66
PU/gelatin/SPIO 3DP	54.0	126.0	12.2	8.32	9.91

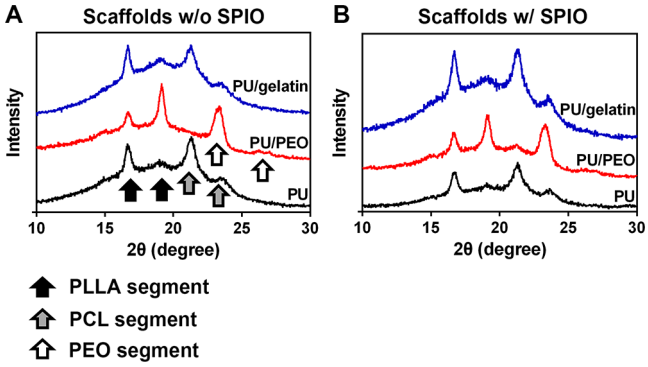

Figure 4. XRD profiles for (A) PU FD, PU/gelatin, and PU/PEO 3DP scaffolds and (B) PU/SPIO FD, PU/PEO/SPIO, and PU/gelatin/SPIO 3DP scaffolds.

Table 2. Dynamic Mechanical Properties of the 3DP Scaffolds at 37 °C

sample	storage modulus E' (kPa)	loss modulus E'' (kPa)	tan δ (E''/E')
PU/PEO 3DP	226 ± 12.2	28.4 ± 0.2	0.126 ± 0.007
PU/PEO/SPIO 3DP	320 ± 39.4	48.9 ± 10.4	0.152 ± 0.014
PU/gelatin 3DP	195 ± 43.2	18.2 ± 3.7	0.094 ± 0.002
PU/gelatin/SPIO 3DP	227 ± 24.1	24.9 ± 2.7	0.110 ± 0.001

dynamical mechanical properties at 37 °C at wet state are shown in Table S1. After immersion in PBS, E' slightly increased for PU/PEO and PU/gelatin scaffolds, while E'' significantly increased. Meanwhile, E' decreased dramatically for the wet PU/PEO/SPIO and PU/gelatin/SPIO scaffolds. The tan δ values of all scaffolds were raised after immersion in PBS.

The weight loss of each scaffold with time is shown in Figure S3A. The weight of the original scaffolds before the degradation test was defined as 100%. In the first week, all the PEO and gelatin contents in the scaffolds were dissolved out. The weight remaining after the first week was about 76% for PU/PEO and PU/PEO/SPIO scaffolds and about 85% for PU/gelatin and PU/gelatin/SPIO scaffolds. None of the scaffolds showed obvious degradation within 4 weeks. The release of SPIO NPs from PU/PEO/SPIO scaffolds and PU/gelatin/SPIO scaffolds is shown in Figure S3B. The SPIO release from PU/PEO/SPIO scaffolds was faster than that from PU/gelatin/SPIO scaffolds. The total release of SPIO NPs was about 3% of the total SPIO contents in the initial scaffolds, and most SPIO NPs still remained in the scaffolds.

3.4. Shape Memory Performance of the FD and 3DP Scaffolds. In the shape memory tests, the definition of permanent shape, temporary shape, fixed angle, and recovery angle is depicted in Figure 5A. Full schematic description of the

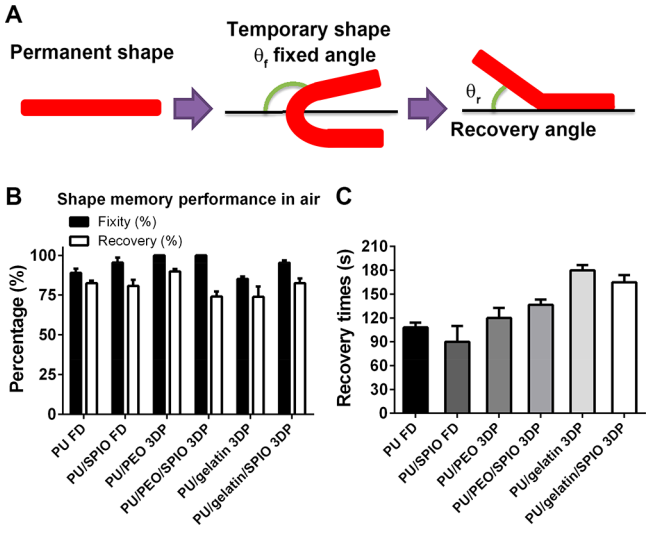

Figure 5. Shape memory properties in 50 °C air condition: (A) definition of the fixed angle and recovery angle for the evaluation of shape memory; (B) fixity and recovery ratios of PU FD and PU/SPIO FD scaffolds, as well as PU/PEO, PU/PEO/SPIO, PU/gelatin, and PU/gelatin/SPIO 3DP scaffolds in air; (C) recovery time for each scaffold to reach the final recovery ratio.

shape memory testing procedures is presented in Figure S4. The shape memory fixity and recovery ratios obtained in 50 °C air by eq 1 and eq 2 in the Materials and Methods section are demonstrated in Figure 5B. The fixity ratio was in the range of 85.2−100%, and the recovery ratio was in the range of 73.9−89.8%. The addition of PEO promoted the fixity for 3DP scaffolds, while the addition of gelatin suppressed it. The addition of SPIO NPs also promoted the shape fixity. The highest fixity was 100% for PU/PEO and PU/PEO/SPIO scaffolds. On the other hand, the shape recovery ratio was not completely correlated with the addition of SPIO NPs. PU/PEO/SPIO 3DP and PU/SPIO FD scaffolds had lower recovery ratios than PU/PEO 3DP and PU FD scaffolds, while PU/gelatin/SPIO 3DP scaffolds had slightly higher recovery ratios than PU/gelatin 3DP scaffolds. The highest shape recovery in the dried state at 37 °C was 89.8% for PU/PEO 3DP scaffolds. The recovery time for scaffolds reaching final recovery ratios in air is shown in Figure 5C. PU/SPIO FD scaffolds had the fastest recovery speed, while PU/gelatin 3DP had the lowest one. PU/PEO, PU/PEO/SPIO 3DP, PU FD, and PU/SPIO FD did not show significant difference in the recovery speed.

The shape memory fixity and recovery ratios of the scaffolds evaluated in 37 °C water are shown in Figure 6A. All scaffolds showed 100% shape fixity. Meanwhile, PU FD, PU/SPIO FD, PU/PEO 3DP, and PU/PEO/SPIO 3DP scaffolds also had 100% recovery. The shape memory properties in water were

DOI: 10.1021/acsbiomaterials.8b00091
ACS Biomater. Sci. Eng. 2018, 4, 1397−1406

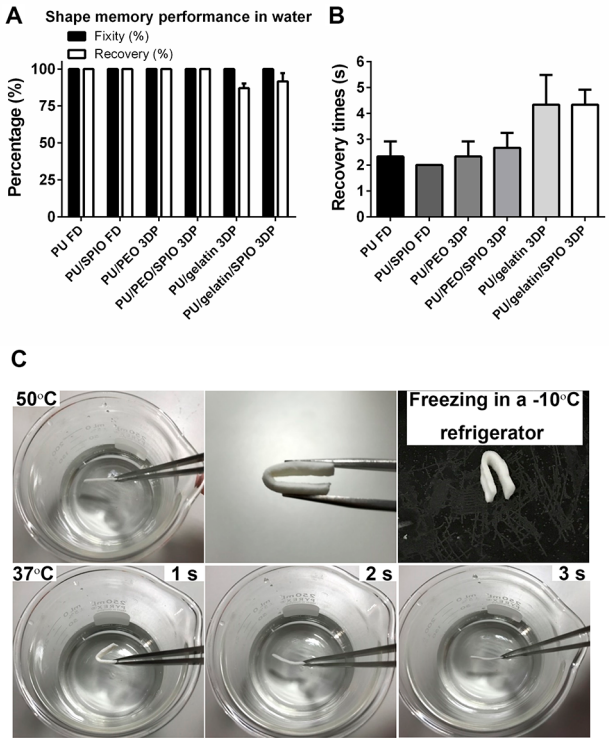

Figure 6. Shape memory properties in 37 °C water condition: (A) fixity and recovery ratios of PU FD and PU/SPIO FD scaffolds, as well as PU/PEO, PU/PEO/SPIO, PU/gelatin, and PU/gelatin/SPIO 3DP scaffolds in water; (B) recovery time for each scaffold to reach the final recovery ratio; (C) continuous images of the PU scaffold showing shape recovery in 37 °C water (using the PU FD scaffolds as an example).

better than that in air. The recovery time for scaffolds reaching final recovery ratios in water is shown in Figure 6B. The shape recovery speed of all scaffolds in water was much faster than that in air, i.e., all within 10 s. PU/SPIO FD had the fastest recovery speed (~2 s), while PU/gelatin and PU/gelatin/SPIO had the slowest one (~4.5 s). These results were consistent with the recovery speed in the dried state. The continuous images of the shape recovery in 37 °C water are shown in Figure 6C. The PU FD scaffold showed 100% recovery and reached the final recovery ratios rather fast.

3.5. Viability of hMSCs Seeded in 3DP Scaffolds. The hMSC seeding process and the cell morphology are shown in Figure 7A,B. hMSCs were seeded in the 3DP scaffolds effectively (>60%). After 24 h, cells in PU/PEO and PU/gelatin 3DP scaffolds formed aggregates. Meanwhile, cells seeded in PU/PEO/SPIO and PU/gelatin/SPIO 3DP scaffolds tended to attach on the stacking fibers of the scaffolds. Cells in PU/PEO and PU/gelatin scaffolds were inclined to grow in the gap areas. The viability of hMSCs is shown in Figure 7C. The cell number in PU/gelatin and PU/gelatin/SPIO 3DP scaffolds obviously increased in 72 h. The cell number of the PU/PEO/SPIO and PU/gelatin/SPIO 3DP scaffolds at 0 h was close to the original cell-seeding number (1.0×10^6), i.e., with high seeding efficiency (80−90%). In PU/PEO/SPIO and PU/gelatin/SPIO 3DP scaffolds, there were more hMSCs staying on the fibers of the scaffolds, while in the PU/PEO and PU/gelatin 3DP scaffolds most of the hMSCs were present in the intervals among fibers.

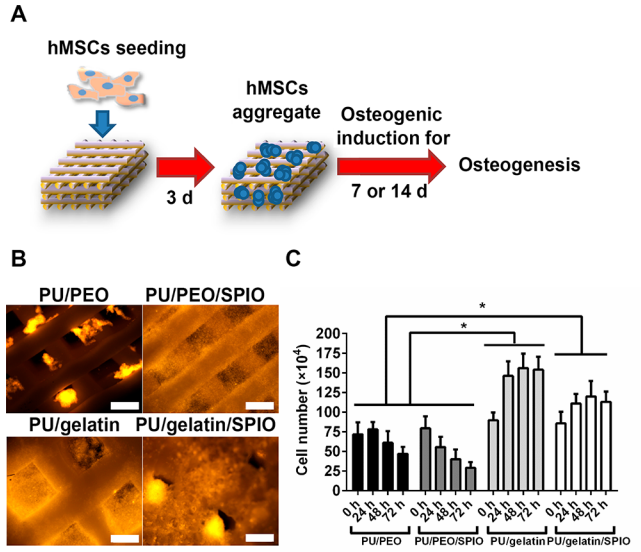

Figure 7. 3DP shape memory scaffolds seeded with hMSCs. (A) Schematics of seeding procedures. (B) Fluorescent images of hMSCs in 3DP scaffolds after 24 h of culture. Cells were labeled by PKH26 (red fluorescence). Scale bar, 400 μm. (C) Number of hMSCs cultured in 3DP scaffolds during 72 h culture period: (*) $p < 0.05$ among the indicated groups.

3.6. Osteogenic Induction for hMSCs Seeded in 3DP Scaffolds. The osteogenic gene marker expression after 7 or 14 days induction is shown in Figure 8. PU/PEO/SPIO constructs demonstrated much greater expression than PU/PEO in ALP, RUNX2, and COL I gene markers and so did PU/gelatin/SPIO vs PU/gelatin. The gene marker expression after 7 days without osteogenic induction is shown in Figure S5

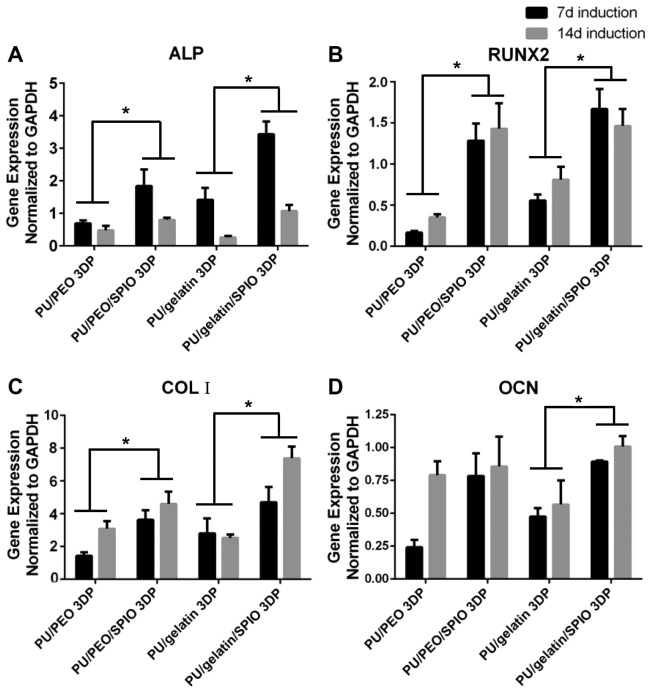

Figure 8. Gene expression for hMSCs grown in 3DP shape memory scaffolds with osteogenic induction for 7 or 14 days: (A) ALP; (B) RUNX2; (C) COL I; (D) OCN. (*) $p < 0.05$ among the indicated groups.

DOI: 10.1021/acsbiomaterials.8b00091
ACS Biomater. Sci. Eng. 2018, 4, 1397−1406

for comparison. The early gene marker ALP upregulated in 7 days with induction and downregulated in 14 days with induction. RUNX2, OCN, and COL I gene markers were upregulated significantly after 7 and 14 days of induction. The ALP and OCN gene expressions without osteogenic induction in PU/gelatin/SPIO were much greater than those in PU/gelatin and so was PU/PEO/SPIO vs PU/PEO (Figure S5).

The cell number in 3DP scaffolds after 14 days of induction is shown in Figure 9A. The cell numbers in PU/PEO (4.8×10^5) and PU/PEO/SPIO (4.1×10^5) scaffolds were lower than those in PU/gelatin (6.9×10^5) and PU/gelatin/SPIO (6.0×10^5) scaffolds. The collagen contents in scaffolds after 14 days of induction are shown in Figure 9B. The collagen contents in PU/PEO/SPIO and PU/gelatin/SPIO scaffolds were much greater than those in PU/PEO and PU/gelatin scaffolds. The quantitative data for calcium deposition in 3DP scaffolds at the end of induction are shown in Figure 9C. PU/PEO/SPIO had the most calcium deposition of all scaffolds (~230 μg). The mineral deposition in PU/gelatin (~158 μg) and PU/gelatin/SPIO (~172 μg) did not show significant difference. The calcium deposition in PU/PEO scaffolds (~140 μg) was much lower than that in PU/PEO/SPIO scaffolds. The mineral deposition stained by Alizarin red is shown in Figure S6. The hMSCs seeded in each of the 3DP scaffolds presented obvious calcium deposition in 14 days. The deposition in PU/PEO and PU/gelatin 3DP scaffolds occurred in the gap areas between the stacking fibers of 3DP scaffolds, which was consistent with the PKH26 images at 24 h. The minerals in PU/PEO/SPIO and PU/gelatin/SPIO 3DP scaffolds were deposited along the stacking fibers as flakes.

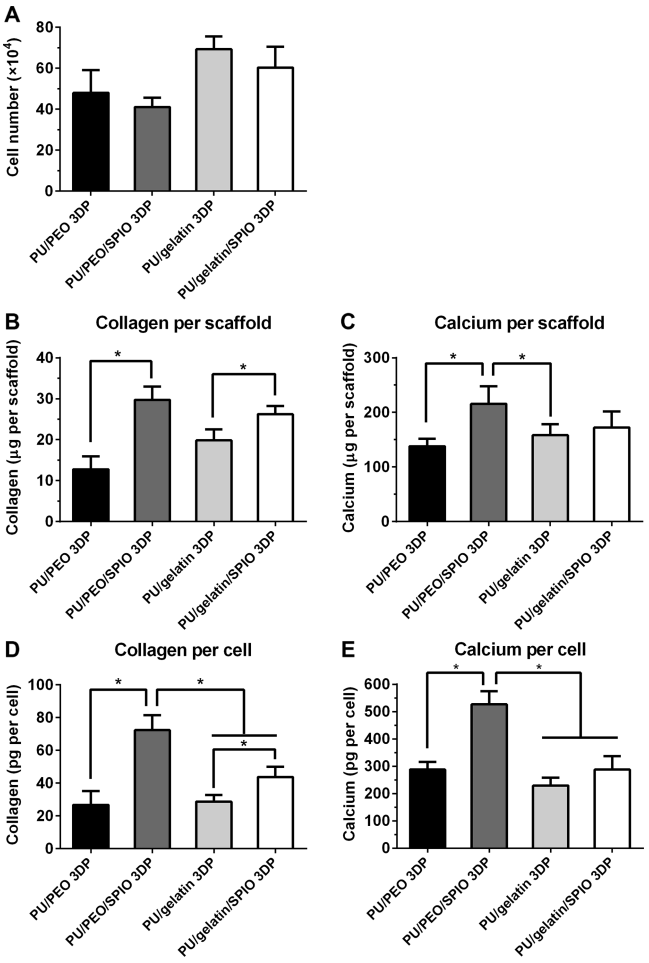

Figure 9. Long-term culture of hMSCs-seeded 3DP shape memory scaffolds: (A) cell numbers in 3DP scaffolds cultured in osteogenic medium for 14 days; (B) Ttotal collagen contents in 3DP scaffolds; (C) total calcium deposition quantified by atomic absorption spectroscopy; (D) collagen secretion per cell; (E) calcium secretion per cell. (*) $p < 0.05$ among the indicated groups.

The collagen contents per cell are shown in Figure 9D. Data were derived from collagen contents per scaffold normalized to cell number. Collagen secreted by hMSCs in PU/gelatin/SPIO (~45.5 pg) scaffolds was much more than that in PU/gelatin (~28.6 pg) and PU/PEO (~26.4 pg) scaffolds. Collagen secretion in PU/PEO/SPIO (~75.2 pg) was the highest of all scaffolds. The quantitative data for calcium deposition per cell are shown in Figure 9E. The mineral deposition in PU/PEO, PU/PEO/SPIO, PU/gelatin, and PU/gelatin SPIO per cell was about 285 pg, 557 pg, 228 pg, and 285 pg, respectively. Cells grown in PU/PEO/SPIO scaffolds had the greatest mineral deposition. Taken together, cells in PU/PEO/SPIO scaffolds showed the most significant osteogenesis after 14 days.

4. DISCUSSION

We developed PU 3D printing ink containing PEO to adjust the viscosity for printability[23] and tuned the ratios of soft segments in PU to achieve the shape memory properties as described in our previous study.[14] Tissue engineering 3DP scaffolds with shape memory properties were thus fabricated based on the PU−PEO ink. In addition, a PU−gelatin ink was created for comparison in this study. Gelatin is biodegradable and has good biocompatibility.[31] The gelatin-based sponge with BMP-2 could promote the repair of bone defects.[32] Moreover, the gelatin-based ink was sensitive to temperature so that we could change the temperature to obtain the viscosity suitable for printing. Both inks showed excellent printability in 3D printing. All the scaffolds showed good printability, and PU/gelatin and PU/gelatin/SPIO 3DP scaffolds could be printed on a platform set above 0 °C (at ~5 °C). The addition of SPIO NPs in the ink made the color of ink brown, while the printability of the ink was not influenced. SPIO NPs are widely used as the MRI contrast agent.[33] With the addition of SPIO NPs, the 3DP scaffolds could be tracked without invasive assessment. An appropriate scaffold for tissue engineering should provide an environment promoting the proliferation and differentiation of MSCs and have interconnected porosity for waste and nutrient transport.[34] The 3DP scaffolds we fabricated showed porous structure, which promoted the metabolism of hMSCs seeded in 3DP scaffolds.

A new mechanism of shape memory PCL−PLLA-based PU was brought to light in our previous work.[14] The orientation of the crystalline PCL segments and PLLA segments rather than overall crystallinity played an important role in the shape memory properties of the PU. During the deforming process, the original PCL and PLLA crystalline domains were aligned, which fixed the shape at a temporary state. Greater overall crystallinity should lead to greater shape fixity based on this theory, and the result of shape fixity in 37 °C air was consistent with the theory. On the other hand, the shape recovery depended on the amorphous PCL segments to recover above the switching temperature, but the deformation induced the amorphous PCL to become oriented crystalline PCL, which was irreversible; i.e., the PCL crystallinity would suppress the shape recovery. The respective crystallinity of PCL and PLLA

DOI: 10.1021/acsbiomaterials.8b00091
ACS Biomater. Sci. Eng. 2018, 4, 1397−1406

segments of the current PU system is listed in Table S2. The addition of SPIO NPs elevated the overall crystallinity and therefore increased the shape fixity ratios. The shape recovery ratios were not elevated by the addition of SPIO NPs and even decreased. In all scaffolds, the PCL crystallinity was increased by the presence of SPIO, except in PU/gelatin/SPIO 3DP scaffolds where only the PLLA crystallinity was increased. The second cycle of DSC curves for each scaffold is shown in Figure S7. The second cycle eliminated the processing history and presented the original characteristics of the materials. Here PCL melting peaks did not show up in the second cycle, which suggested that the PCL crystallinity was produced by the freeze-dried processing. The shape fixity and recovery ratios in 50 °C air of each casting film are shown in Table S3. The films presented a better recovery but worse fixing ability than that of 3DP scaffolds in general. The exceptions were the PU/PEO and PU groups, where the films of the former showed a lower recovery than the scaffolds and the films of the latter showed a better fixing ability than the scaffolds. The different shape memory properties between films and 3DP scaffolds were caused by the difference in PCL crystallinity. These findings indicated that the processing of the materials also critically influenced the shape memory properties through variation of crystallinity.

To illustrate the effect of the microstructure on shape memory properties, we conducted the small-angle X-ray scattering (SAXS) analysis of each scaffold as shown in Figure S8. We could identify the folding state and flexibility of the microstructure by the Kratky method.[35] In regions of high scattering vector ($\mathbf{q}$), the intensity of PU/PEO and PU/gelatin 3DP scaffolds increased as the temperature increased. We proposed that the chain of PU was folded at low temperatures. When the temperature increased, the configuration turned into the unfolded state and became flexible.[36] As the chain configuration disentangled, PU intended to recover its shape. On the other hand, the chain configuration of PU/PEO/SPIO and PU/gelatin/SPIO scaffolds hardly changed as the temperature varied, which was verified by the little change of the SAXS intensity as the temperature increased. We concluded that the presence of SPIO in PU had made the chain configuration more thermally stable and stiff. Therefore, PU with SPIO became more difficult to recover its shape.

Since the 3DP scaffolds were designed for the use in tissue engineering, we further evaluated the shape memory properties in 37 °C water to stimulate the environment in human body. The 3DP scaffolds had porous structure to absorb water. As the 3DP scaffolds were put in 37 °C water, the water may diffuse into the surface pores of the scaffolds even after wiping off the excess water. At the fixity stage in a −10 °C fridge, the water locked in the scaffolds froze and was in favor of the shape fixity. At the recovery stage, the scaffolds were put into 37 °C water again. The water provided secondary force (hydrogen bond) for interaction with PU. This interaction may interfere with the oriented crystalline soft segments that formed during deformation of the scaffolds and weaken the interaction between crystalline domains.[14] Subsequently, the shape of PU recovered to the permanent shape faster and greater in 37 °C water than in 50 °C air.

Tissue engineering had become a trend for the repair of damaged tissue. The main factors of tissue engineering are scaffolds, seeded cells (such as MSCs), and biomolecules.[37] Recent studies revealed that nanoparticles such as silver[38] and gold nanoparticles promoted the osteogenesis.[39,40] Herein, we chose SPIO NPs to blend with printing ink and observed the proliferation and osteogenesis of the hMSCs seeded in 3DP scaffolds. The proliferation of the hMSCs in PU/gelatin and PU/gelatin/SPIO was greater than that in PU/PEO and PU/PEO/SPIO scaffolds. This finding confirmed that gelatin had better biocompatibility than PEO as the viscosity enhancer of the ink. The expression of osteogenic marker genes in PU/PEO/SPIO and PU/gelatin/SPIO after 7 or 14 days induction was greater than that in PU/PEO and PU/gelatin scaffolds. Meanwhile, the osteogenic gene expression did not show significant difference between PU/PEO/SPIO and PU/gelatin/SPIO nor between PU/PEO and PU/gelatin. Therefore, PEO and gelatin as the viscosity enhancer of the ink did not significantly affect the osteogenesis, while the addition of SPIO NPs did. Similar tendencies were observed in collagen secretion and calcium deposition per cell. The addition of SPIO NPs altered the physicochemical properties such as mechanical properties, hydrophobicity, and crystallinity, which might influence the osteogenesis of MSCs.[41,42] The water contact angle and the dynamic mechanical properties of the scaffolds in the wet state are listed in Table S1. The contact angle was related to surface roughness. It was reported that the topography and surface roughness of materials could affect the cellular response.[43] The contact angle of PU/PEO and PU/gelatin scaffolds was 77.8° and 60.2°, respectively. The value decreased to 53.0° by adding SPIO in PU/PEO, while it increased to 75.4° by adding SPIO in PU/gelatin. The osteogenesis of MSCs thus seemed not related to the hydrophobicity of the scaffolds. In the wet state, the storage modulus (E') of PU/PEO/SPIO and PU/gelatin/SPIO scaffolds decreased significantly, while PU/PEO and PU/gelatin scaffolds changed only slightly.

Another key factor to affect the osteogenesis may be the release of SPIO from the scaffolds. The osteogenic gene markers for cells in PU/PEO/SPIO and PU/gelatin/SPIO scaffolds after 7 days without osteogenic induction had already shown greater expression than those of scaffolds without SPIO. The gradual release of SPIO NPs from the scaffolds is shown in Figure S3B. SPIO was released faster from PU/PEO/SPIO and in a larger amount than that from PU/gelatin/SPIO, consistent with the greater expression of the osteogenic genes for PU/PEO/SPIO scaffolds vs PU/gelatin/SPIO scaffolds after 7 days. Combining the above observations, we speculated that the SPIO release from the scaffolds promoted the osteogenesis of hMSCs seeded in the scaffolds. To support this, we cultured hMSCs on TCPS with different concentrations of SPIO NPs and examined the osteogenic gene expression (Figure S9). As the SPIO concentration was higher, the gene expression of RUNX2, COLI, and OCN expression was also higher, except that at low concentrations (15 and 20 ppm) the effect was not so significant. Agreeing with our observation, Wang et al.[20] recently reported that iron oxide promoted the osteogenesis through the activation of MAPK signaling pathway.

Finally, 3D printed scaffolds with shape memory properties and osteogenic effect were designed and fabricated in this study. These scaffolds were incorporated with SPIO and may be tracked by MRI. Meanwhile, SPIO NPs could be heated under the magnetic field,[44] and we could heat the scaffolds by the magnetic field so the inclusion of SPIO NPs was a means to trigger the shape recovery. To demonstrate the feasibility, we conducted the magnetic heating with PU/PEO/SPIO printing ink, and the heating curve is shown in Figure S10. The actual content of the SPIO in printing ink was 100 ppm. The

DOI: 10.1021/acsbiomaterials.8b00091
ACS Biomater. Sci. Eng. 2018, 4, 1397−1406

temperature elevation was valid but somewhat slow (~0.3 °C/min). Besides, we conducted a defect filling experiment to evaluate the feasibility for use in the minimally invasive surgery. PU/gelatin/SPIO scaffolds were heated in 37 °C water bath, compressed from 9 mm to 5 mm, and fixed in a −10 °C refrigerator. After 5 min fixity, the scaffolds were then put into the defect site and performed the recovery in the 37 °C water bath. The shape recovery process of the scaffolds in situ is shown in Figure S11. The scaffolds recovered to 7 mm in 75 s and to 8.5 mm in 180 s. There was no further recovery after 180 s. The volume of the scaffolds was reduced 44% during deformation and fixity (9 × 9 × 2.42 mm^3 to 9 × 5 × 2.42 mm^3) and recovered to 94.4% (9 × 5 × 2.42 mm^3 to 9 × 8.5 × 2.42 mm^3), demonstrating the potential to expand in situ for use in the minimally invasive surgery. In the future, the scaffolds can be designed to have a switching temperature higher than 37 °C and the SPIO contents can be optimized for the magnetic heating to trigger the shape memory in situ. Chemokines such as stromal-derived factor-1 (SDF-1) that induces migration of stem cells[45] may be further added in the ink to produce shape memory 3DP scaffolds as a defected-bone substitute without stem cells. This substitute may be delivered to the site by the minimally invasive surgery and designed to expand in the defected site by magnetic heating. The design concept of such a smart bone scaffold would echo so-called "4D printing".[46]

5. CONCLUSION

We fabricated biodegradable, shape memory PU−PEO and PU−gelatin 3DP scaffolds by the LFDM platform for bone tissue engineering. The optimized printing ink showed good printability. The PU−PEO 3DP scaffolds showed better shape memory properties, while PU−gelatin 3DP scaffolds showed better cell viability. The addition of SPIO NPs enhanced the crystallinity for both PCL and PLLA segments of PU, increasing the shape fixity ratios. The shape recovery ratios depended on the amorphous PCL segments in PU, so SPIO was not directly related to the shape recovery. Shape memory properties in water were influenced by the water uptake of the scaffolds. Water locked in pores helped the shape fixity at −10 °C and interfered with the oriented crystallinity during processing, therefore facilitating the shape recovery. Meanwhile, SPIO release from the PU-based 3DP scaffolds promoted the osteogenesis of the hMSCs in scaffolds and the secretion and deposition of collagen and calcium. Shape memory scaffolds as smart materials fabricated by 3D printing represent a novel category of scaffolds, with the design concept echoing the 4D printing. These novel scaffolds may become potential candidates for applications in the minimally invasive surgery as customized-bone substitutes for bone tissue regeneration.

■ ASSOCIATED CONTENT

Supporting Information

The Supporting Information is available free of charge on the ACS Publications website at DOI: 10.1021/acsbiomaterials.8b00091.

SPIO synthesis process and characterization, SEM images of 3DP scaffolds, degradation and SPIO release of scaffolds, evaluation of shape memory properties, gene expression of hMSCs for 7 days without osteogenic induction, Alizarin red staining of scaffolds, DSC and SAXS profiles, gene expression of hMSCs cultured with different concentrations of SPIO NPs for 7 days, SPIO-containing PU−PEO ink heated under magnetic field, and the process of defect filling by PU/gelatin/SPIO scaffolds in 37 °C water bath (PDF)

■ AUTHOR INFORMATION

Corresponding Author

*Phone: +886-2-3366-5313. Fax: +886-2-3366-5237. E-mail: shhsu@ntu.edu.tw.

ORCID

U-Ser Jeng: 0000-0002-2247-5061

Shan-hui Hsu: 0000-0003-3399-055X

Notes

The authors declare no competing financial interest.

■ ACKNOWLEDGMENTS

This work was funded by the Ministry of Science and Technology (MOST Grants 106-3114-E-002-019 and 106-2221-E-002-079-MY2), Taiwan, R.O.C. We also thank National Synchrotron Radiation Research Center (Grant 2016-1-141-3) and the staff for providing the resources and technical support.

■ REFERENCES

(1) Berg, G. J.; McBride, M. K.; Wang, C.; Bowman, C. N. New directions in the chemistry of shape memory polymers. *Polymer* **2014**, *55* (23), 5849−5872.

(2) Small, W., IV; Singhal, P.; Wilson, T. S.; Maitland, D. J. Biomedical applications of thermally activated shape memory polymers. *J. Mater. Chem.* **2010**, *20* (17), 3356−3366.

(3) Small, W.; Metzger, M. F.; Wilson, T. S.; Maitland, D. J. Laser-activated shape memory polymer microactuator for thrombus removal following ischemic stroke: preliminary in vitro analysis. *IEEE J. Sel. Top. Quantum Electron.* **2005**, *11* (4), 892−901.

(4) Eisenberg, M. J. Drug-Eluting Stents. *Circulation* **2006**, *114* (16), 1745−1754.

(5) Lendlein, A.; Langer, R. Biodegradable, elastic shape-memory polymers for potential biomedical applications. *Science* **2002**, *296* (5573), 1673−1676.

(6) Nakasima, A.; Hu, J. R.; Ichinose, M.; Shimada, H. Potential application of shape memory plastic as elastic material in clinical orthodontics. *Eur. J. Orthod.* **1991**, *13* (3), 179−186.

(7) Fuchs, K. Minimally invasive surgery. *Endoscopy* **2002**, *34* (02), 154−159.

(8) Eberhart, R. C.; Su, S.-H.; Nguyen, K. T.; Zilberman, M.; Tang, L.; Nelson, K. D.; Frenkel, P. Bioresorbable polymeric stents: current status and future promise. *J. Biomater. Sci., Polym. Ed.* **2003**, *14* (4), 299−312.

(9) Wu, G.-H.; Hsu, S.-h. polymeric-based 3D printing for tissue engineering. *J. Med. Biol. Eng.* **2015**, *35* (3), 285−292.

(10) Inzana, J. A.; Olvera, D.; Fuller, S. M.; Kelly, J. P.; Graeve, O. A.; Schwarz, E. M.; Kates, S. L.; Awad, H. A. 3D printing of composite calcium phosphate and collagen scaffolds for bone regeneration. *Biomaterials* **2014**, *35* (13), 4026−4034.

(11) Tarafder, S.; Balla, V. K.; Davies, N. M.; Bandyopadhyay, A.; Bose, S. Microwave-sintered 3D printed tricalcium phosphate scaffolds for bone tissue engineering. *J. Tissue Eng. Regener. Med.* **2013**, *7* (8), 631−641.

(12) Chen, Q.; Liang, S.; Thouas, G. A. Elastomeric biomaterials for tissue engineering. *Prog. Polym. Sci.* **2013**, *38* (3), 584−671.

(13) Hung, K.-C.; Tseng, C.-S.; Dai, L.-G.; Hsu, S.-h. Water-based polyurethane 3D printed scaffolds with controlled release function for customized cartilage tissue engineering. *Biomaterials* **2016**, *83*, 156−168.

(14) Chien, Y.-c.; Chuang, W.-T.; Jeng, U.-S.; Hsu, S.-h. Preparation, Characterization, and Mechanism for Biodegradable and Biocompatible Polyurethane Shape Memory Elastomers. *ACS Appl. Mater. Interfaces* **2017**, *9* (6), 5419−5429.

(15) Bose, S.; Roy, M.; Bandyopadhyay, A. Recent advances in bone tissue engineering scaffolds. *Trends Biotechnol.* **2012**, *30* (10), 546−554.
(16) Bao, M.; Lou, X.; Zhou, Q.; Dong, W.; Yuan, H.; Zhang, Y. Electrospun biomimetic fibrous scaffold from shape memory polymer of PDLLA-co-TMC for bone tissue engineering. *ACS Appl. Mater. Interfaces* **2014**, *6* (4), 2611−2621.
(17) Li, T.-J.; Huang, C.-C.; Ruan, P.-W.; Chuang, K.-Y.; Huang, K.-J.; Shieh, D.-B.; Yeh, C.-S. In vivo anti-cancer efficacy of magnetite nanocrystal-based system using locoregional hyperthermia combined with 5-fluorouracil chemotherapy. *Biomaterials* **2013**, *34* (32), 7873−7883.
(18) Gupta, A. K.; Gupta, M. Synthesis and surface engineering of iron oxide nanoparticles for biomedical applications. *Biomaterials* **2005**, *26* (18), 3995−4021.
(19) Cho, E. C.; Glaus, C.; Chen, J.; Welch, M. J.; Xia, Y. Inorganic nanoparticle-based contrast agents for molecular imaging. *Trends Mol. Med.* **2010**, *16* (12), 561−573.
(20) Wang, Q.; Chen, B.; Cao, M.; Sun, J.; Wu, H.; Zhao, P.; Xing, J.; Yang, Y.; Zhang, X.; Ji, M.; Gu, N. Response of MAPK pathway to iron oxide nanoparticles in vitro treatment promotes osteogenic differentiation of hBMSCs. *Biomaterials* **2016**, *86*, 11−20.
(21) Kalita, H.; Karak, N. Hyperbranched polyurethane/Fe_3O_4 thermosetting nanocomposites as shape memory materials. *Polym. Bull.* **2013**, *70* (11), 2953−2965.
(22) Cai, Y.; Jiang, J. S.; Zheng, B.; Xie, M. R. Synthesis and properties of magnetic sensitive shape memory Fe_3O_4/poly (ε-caprolactone)-polyurethane nanocomposites. *J. Appl. Polym. Sci.* **2013**, *127* (1), 49−56.
(23) Hung, K. C.; Tseng, C. S.; Hsu, S. h. Synthesis and 3D Printing of Biodegradable Polyurethane Elastomer by a Water-Based Process for Cartilage Tissue Engineering Applications. *Adv. Healthcare Mater.* **2014**, *3* (10), 1578−1587.
(24) Sun, J.; Zhou, S.; Hou, P.; Yang, Y.; Weng, J.; Li, X.; Li, M. Synthesis and characterization of biocompatible Fe_3O_4 nanoparticles. *J. Biomed. Mater. Res., Part A* **2007**, *80A* (2), 333−341.
(25) Li, Y.; Chen, H.; Liu, D.; Wang, W.; Liu, Y.; Zhou, S. pH-Responsive Shape Memory Poly (ethylene glycol)−Poly (ε-caprolactone)-based Polyurethane/Cellulose Nanocrystals Nanocomposite. *ACS Appl. Mater. Interfaces* **2015**, *7* (23), 12988−12999.
(26) Kuo, Y.-C.; Hung, S.-C.; Hsu, S.-h. The effect of elastic biodegradable polyurethane electrospun nanofibers on the differentiation of mesenchymal stem cells. *Colloids Surf., B* **2014**, *122*, 414−422.
(27) Kim, Y.-J.; Sah, R. L.; Doong, J.-Y. H.; Grodzinsky, A. J. Fluorometric assay of DNA in cartilage explants using Hoechst 33258. *Anal. Biochem.* **1988**, *174* (1), 168−176.
(28) Gregory, C. A.; Gunn, W. G.; Peister, A.; Prockop, D. J. An Alizarin red-based assay of mineralization by adherent cells in culture: comparison with cetylpyridinium chloride extraction. *Anal. Biochem.* **2004**, *329* (1), 77−84.
(29) Reddy, G. K.; Enwemeka, C. S. A simplified method for the analysis of hydroxyproline in biological tissues. *Clin. Biochem.* **1996**, *29* (3), 225−229.
(30) Smith, J. G.; Sams, W. M.; Davidson, E. A.; Clark, R. D. Pseudoxanthoma elasticum: histochemical and biochemical alterations. *Arch. Dermatol.* **1962**, *86* (6), 741−744.
(31) Li, D.; Sun, H.; Jiang, L.; Zhang, K.; Liu, W.; Zhu, Y.; Fangteng, J.; Shi, C.; Zhao, L.; Sun, H.; Yang, B. Enhanced biocompatibility of PLGA nanofibers with gelatin/nano-hydroxyapatite bone biomimetics incorporation. *ACS Appl. Mater. Interfaces* **2014**, *6* (12), 9402−9410.
(32) Yamamoto, M.; Hokugo, A.; Takahashi, Y.; Nakano, T.; Hiraoka, M.; Tabata, Y. Combination of BMP-2-releasing gelatin/β-TCP sponges with autologous bone marrow for bone regeneration of X-ray-irradiated rabbit ulnar defects. *Biomaterials* **2015**, *56*, 18−25.
(33) Jin, R.; Lin, B.; Li, D.; Ai, H. Superparamagnetic iron oxide nanoparticles for MR imaging and therapy: design considerations and clinical applications. *Curr. Opin. Pharmacol.* **2014**, *18*, 18−27.
(34) Kim, M. S.; Kim, J. H.; Min, B. H.; Chun, H. J.; Han, D. K.; Lee, H. B. Polymeric scaffolds for regenerative medicine. *Polym. Rev.* **2011**, *51* (1), 23−52.
(35) Bernadó, P.; Blackledge, M. A self-consistent description of the conformational behavior of chemically denatured proteins from NMR and small angle scattering. *Biophys. J.* **2009**, *97* (10), 2839−2845.
(36) Pollack, L.; Tate, M. W.; Darnton, N. C.; Knight, J. B.; Gruner, S. M.; Eaton, W. A.; Austin, R. H. Compactness of the denatured state of a fast-folding protein measured by submillisecond small-angle x-ray scattering. *Proc. Natl. Acad. Sci. U. S. A.* **1999**, *96* (18), 10115−10117.
(37) Langer, R.; Vacanti, J. Tissue engineering. *Science* **1993**, *260* (5110), 920−926.
(38) Zhang, R.; Lee, P.; Lui, V. C.; Chen, Y.; Liu, X.; Lok, C. N.; To, M.; Yeung, K. W.; Wong, K. K. Silver nanoparticles promote osteogenesis of mesenchymal stem cells and improve bone fracture healing in osteogenesis mechanism mouse model. *Nanomedicine* **2015**, *11* (8), 1949−1959.
(39) Li, J.; Kawazoe, N.; Chen, G. Gold nanoparticles with different charge and moiety induce differential cell response on mesenchymal stem cell osteogenesis. *Biomaterials* **2015**, *54*, 226−236.
(40) Yi, C.; Liu, D.; Fong, C.-C.; Zhang, J.; Yang, M. Gold nanoparticles promote osteogenic differentiation of mesenchymal stem cells through p38 MAPK pathway. *ACS Nano* **2010**, *4* (11), 6439−6448.
(41) Murphy, C. M.; Matsiko, A.; Haugh, M. G.; Gleeson, J. P.; O'Brien, F. J. Mesenchymal stem cell fate is regulated by the composition and mechanical properties of collagen−glycosaminoglycan scaffolds. *J. Mech. Behav. Biomed. Mater.* **2012**, *11*, 53−62.
(42) Kalbacova, M.; Broz, A.; Kong, J.; Kalbac, M. Graphene substrates promote adherence of human osteoblasts and mesenchymal stromal cells. *Carbon* **2010**, *48* (15), 4323−4329.
(43) Dalby, M. J.; Gadegaard, N.; Tare, R.; Andar, A.; Riehle, M. O.; Herzyk, P.; Wilkinson, C. D.; Oreffo, R. O. The control of human mesenchymal cell differentiation using nanoscale symmetry and disorder. *Nat. Mater.* **2007**, *6* (12), 997−1003.
(44) Fortin, J.-P.; Wilhelm, C.; Servais, J.; Ménager, C.; Bacri, J.-C.; Gazeau, F. Size-sorted anionic iron oxide nanomagnets as colloidal mediators for magnetic hyperthermia. *J. Am. Chem. Soc.* **2007**, *129* (9), 2628−2635.
(45) Takano, T.; Li, Y.-J.; Kukita, A.; Yamaza, T.; Ayukawa, Y.; Moriyama, K.; Uehara, N.; Nomiyama, H.; Koyano, K.; Kukita, T. Mesenchymal stem cells markedly suppress inflammatory bone destruction in rats with adjuvant-induced arthritis. *Lab. Invest.* **2014**, *94* (3), 286.
(46) Khoo, Z. X.; Teoh, J. E. M.; Liu, Y.; Chua, C. K.; Yang, S.; An, J.; Leong, K. F.; Yeong, W. Y. 3D printing of smart materials: A review on recent progresses in 4D printing. *Virtual Phys. Prototyp.* **2015**, *10* (3), 103−122.

DOI: 10.1021/acsbiomaterials.8b00091
ACS Biomater. Sci. Eng. 2018, 4, 1397−1406